

Numerical simulations of necklaces in SU(2) gauge-Higgs field theory

Mark Hindmarsh,^{1,2,*} Kari Rummukainen,^{2,†} and David J. Weir^{2,3,‡}

¹*Department of Physics and Astronomy, University of Sussex, Falmer, Brighton BN1 9QH, U.K.*

²*Department of Physics and Helsinki Institute of Physics, PL 64, FI-00014 University of Helsinki, Finland*

³*Institute of Mathematics and Natural Sciences, University of Stavanger, 4036 Stavanger, Norway*

(Dated: April 4, 2017)

We perform the first numerical simulations of necklaces in a non-Abelian gauge theory. Necklaces are composite classical solutions which can be interpreted as monopoles trapped on strings, rather generic structures in a Grand Unified Theory. We generate necklaces from random initial conditions, modelling a phase transition in the early Universe, and study the evolution. For all cases, we find that the necklace system shows scaling behaviour similar to that of a network of ordinary cosmic strings. Furthermore, our simulations indicate that comoving distance between the monopoles or semipoles along the string asymptotes to a constant value at late times. This means that while the monopole-to-string energy density ratio decreases as the inverse of the scale factor, a horizon-size length of string has a large number of monopoles, significantly affecting the dynamics of string loops. We argue that gravitational wave bounds from millisecond pulsar timing on the string tension in the Nambu-Goto scenario are greatly relaxed.

PACS numbers: 98.80.Cq, 11.15.-q

I. INTRODUCTION

As the early universe cooled and expanded, it may have undergone several symmetry-breaking phase transitions. Depending on the details of the symmetry breaking, it is possible that topological defects could have formed during such phase transitions. Probably the most important class of topological defects for the purposes of cosmology are cosmic strings [1] (see Refs. [2–5] for reviews). These are one-dimensional defects which, in the simplest case of an Abelian Higgs model, arise from the breaking of a U(1) symmetry. The resulting cosmic strings are then extended Nielsen-Olesen vortex lines [6]. Cosmic strings can also arise as fundamental objects from an underlying string theory [7–10].

Abelian Higgs strings have been widely studied, and their observational consequences thoroughly explored [11–15]. Superstrings or field theories with non-Abelian symmetries can produce richer physics: for example, the symmetry-breaking transition $SU(2) \rightarrow Z_N$ has multiple species of strings with N -fold junctions [16]. Networks of strings with junctions have been numerically simulated in Refs. [17–19], and modelled in Refs. [20, 21].

In this paper we report on the first 3-dimensional numerical simulations of a network of strings in a non-abelian gauge theory, one with symmetry-breaking $SU(2) \rightarrow Z_2$ [6, 22–25]. This model is particularly attractive because it can be embedded naturally in Grand Unified Theories (GUTs) such as SO(10) [26], for which cosmic strings are themselves argued to be generic [27]. In addition to the SO(10) case with a single scale, our model permits two symmetry-breaking

scales with an intermediate unbroken U(1) symmetry, modelling a two-stage GUT symmetry-breaking. In this case the first stage, $SU(2) \rightarrow U(1)$, produces 't Hooft-Polyakov monopoles [28, 29], and the second attaches each monopole to two strings, both carrying half the flux. This combination – of a monopole trapped on a cosmic string – is called a bead [22], and if many such beads exist on one string then the configuration is commonly referred to as a necklace [30]. For a review of these systems, see Ref. [31].

In [32] we emphasised the importance of global symmetries in the classification of the beads. In particular, there is a $Z_2 \times Z_2$ symmetry spontaneously broken to Z_2 by the string solutions, and beads can be viewed as the resulting kinks. We discovered new solutions in the case where the SU(2) and U(1) symmetry-breaking scales are degenerate, due to an enlarged discrete global symmetry D_4 . Each bead splits into two “semipoles”, and these four semipoles can annihilate only with the corresponding anti-semipole: in a generic configuration a semipole may not find itself next to its antipole.

The discrete global symmetry can be further promoted to a global O(2) symmetry, which is spontaneously broken by the string solution but not the vacuum. Hence semipoles dissolve and the strings carry persistent global currents, rather like a tube of superfluid.

There is wide disagreement in the literature about how necklaces evolve in the early universe. The necklace network is characterised by two length scales, the average comoving monopole separation ξ_m and the average comoving string separation ξ_s , in terms of which the physical energy densities ρ_m and ρ_s are

$$\rho_m \simeq \frac{M_m}{(a\xi_m)^3}, \quad \rho_s \simeq \frac{\mu}{(a\xi_s)^2}, \quad (1)$$

where μ is the string mass per unit length when monopoles are absent, M_m is the monopole mass and

* m.b.hindmarsh@sussex.ac.uk

† kari.rummukainen@helsinki.fi

‡ david.weir@helsinki.fi

a is the scale factor. Note that the mass of a monopole on a string is generally less than that of a free monopole, so (1) is only an estimate of the extra energy due to the trapped monopoles.

In a normal string network, the string separation is proportional to the horizon distance, so $\xi_s \propto t$, where t is conformal time: this behaviour is known as scaling. In a scaling network, all quantities with dimensions of length (apart from the string width) grow in proportion to the horizon distance.

In a necklace, there is a new dynamically important length scale [30]

$$d_{\text{BV}} = \frac{M_m}{\mu}. \quad (2)$$

The ratio of the monopole energy density to the string energy density $r = \rho_m/\rho_s$ can be written as

$$r = \frac{d_{\text{BV}}}{ad}, \quad (3)$$

where $d = \xi_m^3/\xi_s^2$ is the average comoving separation between monopoles along the string. It was argued in [30] that r should grow, and it was supposed that eventually the average monopole separation should tend to the string width. With this assumption, r would evolve quickly to a maximum value set by the ratio of the two symmetry-breaking scales.

However, it was argued in [33] that this picture underestimates the effect of monopole annihilations, which act to reduce the number of monopoles per unit length of string $1/d$. If monopole annihilation is efficient, their average separation along the string should scale, so $d \propto t$, or equivalently $r \sim d_{\text{BV}}/t_p$, where $t_p \propto at$ is the physical time.

Given that the total density of the necklace network is $(1+r)\mu/(a\xi_s)^2$, there is a very big difference in the two scenarios, and in particular the flux of ultra-high energy cosmic rays, γ -rays and neutrinos coming from monopole annihilation differs by many orders of magnitude. It is clearly important to settle the issue.

We have performed a set of numerical simulations of a network of strings in the $\text{SU}(2) \rightarrow Z_2$ theory (see Fig. 1). They confirm the spontaneous formation of monopoles, semipoles, and supercurrents along with the string network.

We are particularly interested in extracting the asymptotic behaviour of the network with time, as this is essential for extrapolating to cosmological times much later than the defect formation time. Our results support scaling behaviour in the total density of the necklace network; that is, it decreases as t^{-2} , as does a conventional cosmic string network. The string and monopole average separations ξ_s and ξ_m both grow with time, and the ratio of their energy densities r decreases with time. Our simulations, while limited in range, indicate that the mean comoving monopole separation along the string d is approximately constant, and stays the same order of magnitude as its value when the strings form. We also measure

the root mean square (RMS) velocities of both strings and monopoles, finding that both relax to a values of about 0.5. If the string mass scale is the same as the monopole mass scale, the RMS semipole velocity is a little higher than the string RMS velocity, indicating some relative motion.

Necklaces with a constant comoving monopole separation are a new possibility, which has not been considered before. In the conclusions we briefly discuss how such a network would alter the predictions for important observational signals.

II. THE MODEL AND ITS STATIC SOLUTIONS

We study the $\text{SU}(2)$ Georgi-Glashow model with two Higgs fields in a spatially flat Robertson-Walker metric. In comoving coordinates and conformal time, and with scale factor a , the action is

$$\mathcal{S} = \int d^4x \left(-\frac{1}{4} F_{\mu\nu}^a F^{\mu\nu a} + a^2 \sum_n \text{Tr} [D_\mu, \Phi_n][D^\mu, \Phi_n] - a^4 V(\Phi_1, \Phi_2) \right) \quad (4)$$

where $D_\mu = \partial_\mu + igA_\mu$ is the covariant derivative, $A_\mu = A_\mu^a \tau^a$, and $\tau^a = \sigma^a/2$ where σ^a is a Pauli matrix. The Higgs fields Φ_n , $n = 1, 2$, are in the adjoint representation, $\Phi_n = \phi_n^a \tau^a$. Spacetime indices have been raised with the Minkowski metric with mostly negative signature.

The potential is

$$V(\Phi_1, \Phi_2) = m_1^2 \text{Tr} \Phi_1^2 + \lambda (\text{Tr} \Phi_1^2)^2 + m_2^2 \text{Tr} \Phi_2^2 + \lambda (\text{Tr} \Phi_2^2)^2 + \kappa (\text{Tr} \Phi_1 \Phi_2)^2, \quad (5)$$

with λ and κ positive. One could add a $\text{Tr} \Phi_1^2 \text{Tr} \Phi_2^2$ term, and have separate quartic couplings for the fields. However, this would not alter the important dynamical features of the necklace network.

The directions of the vevs are perpendicular, because of the $(\text{Tr} \Phi_1 \Phi_2)^2$ term in the potential. The system therefore undergoes two symmetry-breaking phase transitions, $\text{SU}(2) \rightarrow \text{U}(1) \rightarrow Z_2$. The vacuum expectation values of the two adjoint scalar fields are given by $\text{Tr} \Phi_{1,2}^2 = |m_{1,2}^2|/2\lambda$, or $v_{1,2}^2 = |m_{1,2}^2|/\lambda$. The scalar masses are then $\sqrt{2}m_{1,2}$. Without loss of generality, we can label the scalar fields such that Φ_1 has the larger vacuum expectation value, and is responsible for the first of the symmetry-breakings.

After the first symmetry-breaking, the theory has 't Hooft-Polyakov monopole solutions with mass [34]

$$M_m = \frac{4\pi v_1}{g} f_m \left(\frac{2\lambda}{g^2} \right); \quad f_m(1) \approx 1.238. \quad (6)$$

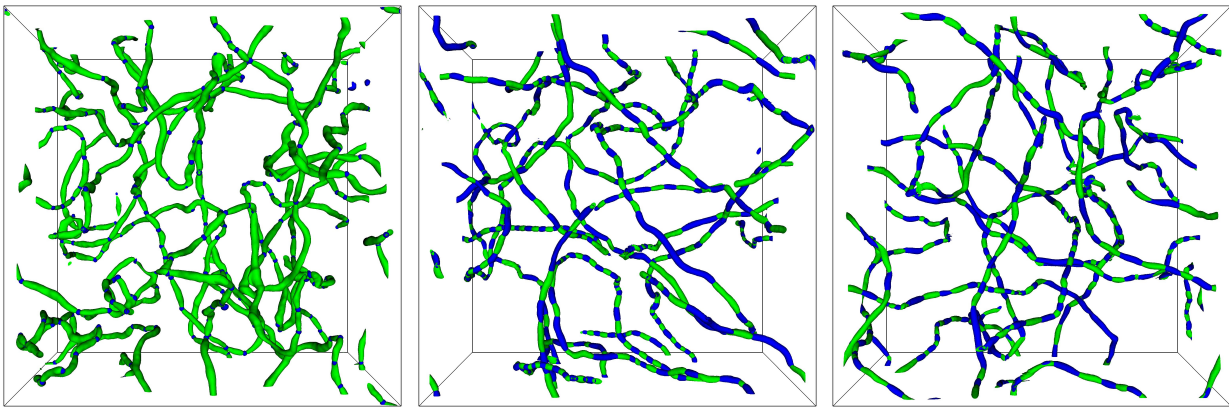


FIG. 1. Views of a small 360^3 simulation for three different parameter choices at $t \approx 240$. The two fields Φ_1 and Φ_2 have blue and green shading respectively. At left, a simulation with $m_1^2 = 0.25$ and $m_2^2 = 0.025$ (contours shown with $\text{Tr} \Phi_1^2 = 0.2$ and $\text{Tr} \Phi_2^2 = 0.04$), giving rise to monopoles (blue) as beads on strings (green). The other two images show a system with $m_1^2 = m_2^2 = 0.25$ (contours shown with $\text{Tr} \Phi^2 = 0.2$ for both Φ_1 and Φ_2). In the centre, $\kappa = 2$, showing the semipoles at the boundaries between the two colours. At right, $\kappa = 1$, and the theory has a continuous global symmetry, meaning that the boundaries between the colours have no extra energy.

After the second symmetry-breaking, the theory has string solutions, with mass per unit length

$$\mu = \pi v_2^2 f_s \left(\frac{2\lambda}{g^2} \right), \quad (7)$$

where $f_s(1) = 1$.

As described in [32], in the generic case $m_1^2 > m_2^2$ this system has a discrete global $Z_2 \times Z_2$ symmetry $\Phi_1 \rightarrow \pm \Phi_1$ and $\Phi_2 \rightarrow \pm \Phi_2$. The string solutions break it down to Z_2 . The resulting kinks interpolating between the two string solutions, called beads [22], can be interpreted as 't Hooft-Polyakov monopoles with their flux confined to two tubes. When $m_1^2 = m_2^2$, the global symmetry is enlarged by the transformation $\Phi_1 \rightarrow \Phi_2$ to D_4 , the square symmetry group, which is broken to Z_2 by strings. The resulting kinks are labelled by a Z_4 topological charge. A pair of these kinks has the same charge as a monopole on a string, hence the name semipole.

Finally, when $m_1^2 = m_2^2$ and $\kappa = \lambda$, there is a global $O(2)$ symmetry

$$\Phi \rightarrow e^{i\alpha} \Phi \quad \text{and} \quad \Phi \rightarrow \Phi^*, \quad (8)$$

where $\Phi = \Phi_1 + i\Phi_2$. The phase of the complexified adjoint scalar θ , defined by $\tan \theta = |\Phi_2|/|\Phi_1|$, changes smoothly along the string. In this case the string supports persistent supercurrents, proportional to the gradient of the phase along the string.

In order to achieve greater dynamic range, it is common practice in cosmic string simulations to scale the couplings and mass parameters with factors a^{1-s} , where a is the cosmological scale factor and $0 \leq s \leq 1$. This is done in such a way as to keep the scalar expectation value fixed. As a result, the physical string width grows for $s < 1$, but the string tension depends only on the ratio of the scalar self coupling to the square of the gauge

coupling, and so stays constant. The dynamics of a string network at $s = 0$ are very similar to those at $s = 1$ [35].

By contrast, the monopole mass M_m is inversely proportional to its radius, and so M_m and the dynamical quantity d_{BV} both grow throughout simulations with $s < 1$. It is therefore not clear how the necklaces should behave in this case: the growing mass might lead one to expect that the monopole RMS velocity should decrease, and the monopole density increase. We will see however that necklaces behave similarly with $s = 0$ as they do with $s = 1$.

III. LATTICE IMPLEMENTATION

A. Discretisation and initial conditions

We simulate the system by setting temporal gauge $A_0 = 0$ and then discretising the system on a comoving 3D spatial lattice. The Hamiltonian of this model in the cosmological background takes the form

$$\begin{aligned} H(t) = & \frac{1}{2g^2 a^{2(s-1)}} \sum_{x,i,a} \epsilon_i^a(x,t)^2 + \frac{1}{2} a^2 \sum_{x;n,a} \pi_n^a(x,t)^2 \\ & + \frac{4}{g^2 a^{2(s-1)}} \sum_{x;i < j} \left(1 - \frac{1}{2} \text{Tr} U_{ij}(x,t) \right) \\ & - a^2 \sum_{x;i,n} 2 \text{Tr} \Phi_n(x) U_i(x) \Phi_n(x + \hat{i}) U_i^\dagger(x) \\ & + a^2 \sum_{x,n} 6 \text{Tr} \Phi_n^2 + a^4 \sum_x V(\Phi_1, \Phi_2) \quad (9) \end{aligned}$$

where the link matrices are $U_\mu = u^0 + i\sigma^a u^a$ with $(u^0)^2 + u^a u^a = 1$ and

$$\epsilon_i^a = -(i/2)\text{Tr}(\sigma^a \dot{U}_i U_i^\dagger). \quad (10)$$

With the time-varying constants, the potential becomes

$$V(\Phi_1, \Phi_2) = \frac{1}{a^{2(1-s)}} [m_1^2 \text{Tr} \Phi_1^2 + \lambda(\text{Tr} \Phi_1^2)^2 + m_2^2 \text{Tr} \Phi_2^2 + \lambda(\text{Tr} \Phi_2^2)^2 + \kappa(\text{Tr} \Phi_1 \Phi_2)^2]. \quad (11)$$

The parameter s can be chosen to be smaller than its physical value 1, in order that the comoving width of the monopoles and strings $w_m \sim (a^s m_1)^{-1}$, $w_s \sim (a^s m_2)^{-1}$, does not shrink below the lattice spacing during the simulation [14]. This extends the time range over which a simulation can be run.

We evolve our lattice equations of motion with a standard Leapfrog method, and the damping term is handled using the Crank-Nicolson method. More details of our numerical methods can be found in Appendix A.

We perform simulations with both $s = 1$ and $s = 0$, with two different expansion rate parameters, defined as

$$\nu = d \ln a / d \ln t. \quad (12)$$

We will see that the quantities of most interest described in the next section behave in similar ways, justifying the use of $s = 0$.

Our initial conditions for $\Phi_{1,2}$ are uniformly distributed random values in the range $[-0.5, 0.5]$ for each component $\phi_{1,2}^a$, while for the SU(2) gauge field on the lattice we generate a random SU(2) matrix from four Gaussian random numbers $\{u^0, u^a\}$ which we then normalise to obtain a unitary matrix of determinant 1.

We first run for a period of time with relatively strong damping ($\sigma = 0.25$, see Appendix A) before switching to standard Hubble damping at $t_{0,H}$ (see Table I). The momenta at the end of the damping phase are about a thousandth the size of those arising initially from the random initial conditions.

The procedure of seeding random fields at each site followed by a period of over-damped evolution is standard for modelling initial conditions for topological defects. The important feature is that the correlations vanish beyond a certain length scale, which is bounded above by the causal horizon [1]. A finite correlation length is a sufficient condition for defects to form. In all numerical experiments to date, the fields subsequently evolve towards a self-similar or scaling configuration which at large distances is independent of the initial conditions. An explicit check of the scaling in Abelian Higgs string simulations with two different sets of initial conditions was made in [15], although see also [36] for a discussion of possible scaling violation by super-horizon correlations in truly thermal initial conditions).

We then run with $s = -1$ for a period until time t_{cg} , during which the comoving string width grows linearly. After t_{cg} , s is set to its physical value $s = 1$. The reason

for this period of core growth is to accelerate the preparation of the string network: the time taken for the fields to settle to their vacua is of order w_m and w_s , so it is helpful to arrange for them to be small while the fields are relaxing. The graphs of w_m and w_s are shown in Appendix B in Fig. 8.

When $\nu = 0$ or when $s = 0$, there is no need for the period of core growth, and data taking can begin at $t_{0,H}$.

Our initial conditions are designed as a compromise between removing unwanted short-distance fluctuations and allowing the strings to form in a reasonable time.

Due to the initial cooling period, the lattice ultraviolet modes remain strongly suppressed during the evolution of the string network. This is justified physically, because in the early universe the local energy density within the strings is much larger than the energy density of the thermal background (although, in a given volume, the total energy of the thermal background can be larger than the energy of the string network). Thus, the thermal modes are expected to have little influence on the string evolution. This also helps us to avoid the problems associated with the thermal ultraviolet modes in real-time lattice equations of motion [37].

B. Numerical tests

In simulations where expansion and the Hubble damping were turned off ($\nu = 0$), energy conservation was better than 0.1% over the period from $t = t_{0,H} = 42.5$ to $t = 720$. The root mean square per-site relative Gauss law violation $\overline{G}/\overline{\rho}$ never exceeded 3×10^{-15} during our simulations, approaching this value only in the initial heavy damping phase. For more details see Appendix A, and in particular Eq. (A12).

In the expanding case with $s = 1$, comoving energy conservation was obeyed to 0.1% for simulations with $m_1^2 = 0.25$, $m_2^2 = 0.1$, while the relative Gauss law violation $\overline{G}/\overline{\rho}$ was at most 8×10^{-4} , a value reached at the start of the core growth phase.

We also tested whether the lattice spacing was acceptable: if the lattice is too coarse, velocities tend to be reduced as the kinetic energy of a defect can be converted into radiation.¹ For these tests we compared $s = 0$ and $s = 1$ simulations at $m_1^2 = m_2^2 = 0.25$ with those at $m_1^2 = m_2^2 = 0.1$, both with $\kappa = 2$. The string RMS velocities at $s = 1$ differed by about 1% between simulations with different masses, suggesting that any effect of the lattice spacing on the dynamics of the strings is minor. However, with $s = 0$, monopole and semipole RMS velocities were as much as 10% higher at the lower mass, indicating that there is some lattice friction at $m_1^2 = m_2^2 = 0.25$. Our $s = 0$ runs are therefore carried out at $m_1^2 = m_2^2 = 0.1$.

¹ For methods of mitigating this energy loss see Refs. [38, 39].

IV. MEASUREMENTS

A. Network length scale

We measure the number of monopoles N , the string length L , and study length scales derived from them. We obtain the number of monopoles N by computing the residual unbroken $U(1)$ gauge field using projectors derived from Φ_1 , the Higgs field which forms the monopoles. From this, we can compute the divergence of the effective magnetic field and hence the magnetic charge. We give fuller details of the $U(1)$ projection in Appendix C, based on Ref. [40].

We compute the length of string by counting the plaquettes with a gauge-invariant ‘winding’ in the $U(1)$ subgroups formed by projection with the scalar field Φ_1 , which is the heavier one in the non-degenerate case.

The comoving string length L is then defined to be the number of plaquettes with winding. It is possible to include a geometric correction to ξ_s to account for the fact that counting the winding number gives the Manhattan distance along the string rather than the true string length (see Ref. [41]). We choose to omit it, which should be borne in mind when comparing to other field theory simulations [14, 35].

B. Monopole density

Several further quantities can be derived from N and L . First, the average comoving string and monopole separations,

$$\xi_s = (V/L)^{1/2} \quad \text{and} \quad \xi_m = (V/N)^{1/3}. \quad (13)$$

We define the average comoving monopole separation along the string

$$d = L/N = \frac{\xi_m^3}{\xi_s^2}. \quad (14)$$

and the average number of monopoles per comoving length of string

$$n = N/L = 1/d. \quad (15)$$

The quantity r defined in (3) can be thought of as the number of monopoles per unit physical length relative to the length scale d_{BV} . The string and monopole separations can be combined into one network length scale ξ_n , defined as

$$\frac{1}{\xi_n^2} = \frac{1}{\xi_s^2} (1 + r). \quad (16)$$

The energy density of the necklace is proportional to ξ_n^{-2} , and when $r > 1$ the majority of the energy in the network is due to the monopoles.

Note that in the degenerate cases $m_2^2/m_1^2 = 1$ with $\kappa = 1$, the points where Φ_1 vanishes recorded by our

monopole search algorithm are not special: there is no local maximum in the energy density. However, they can be used as convenient markers of the phase θ , defined after Eq. (8).

C. Monopole and string velocities

We use the positions of the strings and monopoles to compute the string root-mean-square (RMS) velocity \bar{v} , and the monopole RMS velocity \bar{v}_m .

Using the projection methods discussed in Appendix C, we record a list of the lattice cells that contain magnetic charge every few timesteps. We then take these lists for two timesteps and form a distance matrix for every pair of monopoles in the system. If the time interval δt is much smaller than ξ_m , we can assume that pairing each monopole at the later timestep with the closest one at the earlier timestep captures the same monopole at two different times. On the other hand, the time interval between measurements has to be large enough that lattice-scale discretisation ambiguities do not induce noise [39]. We will therefore compare results for several different δt .

There are a number of standard algorithms to find the choice of pairings in a distance matrix that minimises the total distance. We used a simple ‘greedy’ algorithm that found the smallest entry in the entire distance matrix, then removed that monopole pair, repeating until all monopoles at the later time were paired up. This algorithm has the advantage of being easy to code, on the other hand it scales as the square of the number of monopoles.

The system has periodic boundary conditions, and so a ‘halo’ region is included from the other side of the lattice to ensure that all possible subluminal monopole separations will be found. Once we have determined all the pairings, we remove spurious superluminal pairings (typically $\lesssim 1\%$ of measurements) and use the results to determine \bar{v}_m . We considered $\delta t = 5, 10$ and 15 and found convergence in the resulting curves. We used $\delta t = 15$ for our results. The difference from $\delta t = 10$ can be considered as a systematic uncertainty, but in practice it is comparable to or smaller than the random error.

For the string velocities, a very similar approach was adopted, using the positions of the plaquettes threaded by string. As many plaquettes can be threaded by the strings in the system, the above pairing and distance finding algorithms were parallelised. Even so, determining the string velocity for a few hundred thousand plaquettes between a pair of timesteps took about five minutes on 120 processors. For this reason, string velocities are not computed at early times, when the number of plaquettes becomes too large. The corresponding monopole measurement takes about a second, and can be performed throughout the simulations.

m_1^2	m_2^2	g	λ	κ	M_m	μ	d_{BV}	ν	$t_{0,\text{H}}$	t_{cg}
0.25	0.25	1	0.5	2	11	1.6	7	1	30	230
0.25	0.25	1	0.5	1	11	1.6	7	1	30	230
0.25	0.1	1	0.5	1	11	0.63	17.5	0.5	42.5	242.5
0.25	0.1	1	0.5	1	11	0.63	17.5	1	42.5	242.5
0.25	0.05	1	0.5	1	11	0.31	35	0.5	60	260
0.25	0.05	1	0.5	1	11	0.31	35	1	60	260

TABLE I. List of parameters for $s = 1$ (physical) runs, with dimensionful parameters given in units of the lattice spacing a . Potential parameters (5) are shown along with the isolated monopole mass M_m and the isolated string tension μ computed using Eqs. (6) and (7). The length scale d_{BV} as computed using Eq. (2) is also shown. Finally, we quote the expansion rate parameter $\nu = d \ln a / d \ln t$, the time at which we change to Hubble damping during our simulations, $t_{0,\text{H}}$, and the time at which core growth ends and strings and monopoles reach their true physical width t_{cg} . All these simulations have lattice size 720 and duration 720.

V. RESULTS

We run over several different parameter choices for both $s = 1$ and $s = 0$.

The parameters cover both the degenerate ($m_1^2 = m_2^2$) and non-degenerate cases, and allow us to explore the three possible global symmetries of the string solutions, namely $O(2)$, D_4 , and $Z_2 \times Z_2$. In the degenerate case three cross-couplings κ are considered: the special case $\kappa = 2\lambda$ having $O(2)$ symmetry, and both $\kappa > 2\lambda$ and $\kappa < 2\lambda$. For the non-degenerate case, having $Z_2 \times Z_2$ symmetry, we explore various ratios of m_1^2 to m_2^2 .

Two different expansion rate parameters $\nu = 0.5, 1$ were chosen, where ν is defined in Eq. (12). The choice $\nu = 1$ represents a radiation-dominated universe. While $\nu = 0.5$ does not correspond to any realistic cosmology, it is useful to explore the impact of different expansion rates. Simulating in a matter dominated background ($\nu = 2$) does not give enough dynamic range for reliable results.

All runs are carried out with $m_1^2 = 0.25$ ($s = 1$) and $m_1^2 = 0.1$ ($s = 0$). The parameter choices are listed in Tables I and II. The scale factor is normalised so that $a = 1$ at the end of the simulation.

The units are defined such that the lattice spacing Δx is 1. All simulations are carried out on a 720^3 lattice, with timestep $\Delta t = 0.25$ after the initial heavy damping period ends at $t_{0,\text{H}}$, for a total time 720, or one light-crossing time of the box. In principle, correlations can start to be established after half a light-crossing time. However, the only massless excitations are waves on the string, and the strings are much longer than the box size even at the end of the simulations. The network length scale does not show any evidence for finite-size effects, although it is possible that the slight increase in d for semipoles and supercurrents at $t \gtrsim 360$ in Fig. 4 is a sign of the limited simulation volume.

m_1^2	m_2^2	g	λ	κ	M_m	μ	d_{BV}	$t_{0,\text{H}}$
0.1	0.1	1	0.5	2	6.96	0.628	11.1	30
0.1	0.1	1	0.5	1	6.96	0.628	11.1	30
0.1	0.1	1	0.5	0.5	6.96	0.628	11.1	30
0.1	0.04	1	0.5	1	6.96	0.251	27.7	67.1
0.1	0.02	1	0.5	1	6.96	0.126	55.4	94.9
0.1	0.01	1	0.5	1	6.96	0.0628	111	134

TABLE II. List of simulation parameters for runs with $s = 0$, as for Table I. The expansion rate parameter is $\nu = 1$ (radiation era) for all simulations. At $s = 0$ the physical size of the monopole and string cores grows in proportion to the scale factor. All these simulations have lattice size 720 and duration 720.

Each set of parameter choices is run for 3 different realisations of the initial conditions, and our results are statistical averages over these runs.

We investigate the monopole density with the two different measures introduced in Section IV, the monopole-to-string density ratio r and the number of monopoles per unit comoving length of string n .

A. Network length scale

In Fig. 2 we plot the comoving necklace network length scale ξ_n , defined in Eq. (16), for $s = 1$ (top) and $s = 0$ (bottom).

All cases show linear growth with time, which means that the network is scaling. We perform fits in the range $360 < t < 480$, which while in excess of the half light crossing time for the system, allows time for the scaling behaviour to develop. There are small differences in the slope between simulations with different mass ratios, although there is not enough dynamic range to ensure that they are not inherited from differences in the initial conditions. There is also evidence that the lower expansion rate $\nu = 1/2$ the slope is lower, i.e. that the average necklace density is higher.

B. Monopole density

In Fig. 3 we plot the ratio of monopole to string energy density r , defined in (3), against time in units of m_1^{-1} , for all parameters given in Table I. Note that m_1^{-1} is approximately the monopole size.

We see that r decreases after the formation of the string network, with what appears to be a power law after the core growth period has finished.

The significance of the power law is clearer if we plot the comoving linear monopole density on the string n , again in units of m_1^{-1} (Fig. 4). We can see from the figure that, with the possible exception of the mass-degenerate cases ($m_2^2/m_1^2 = 1$) at $s = 1$, n appears to tend to a

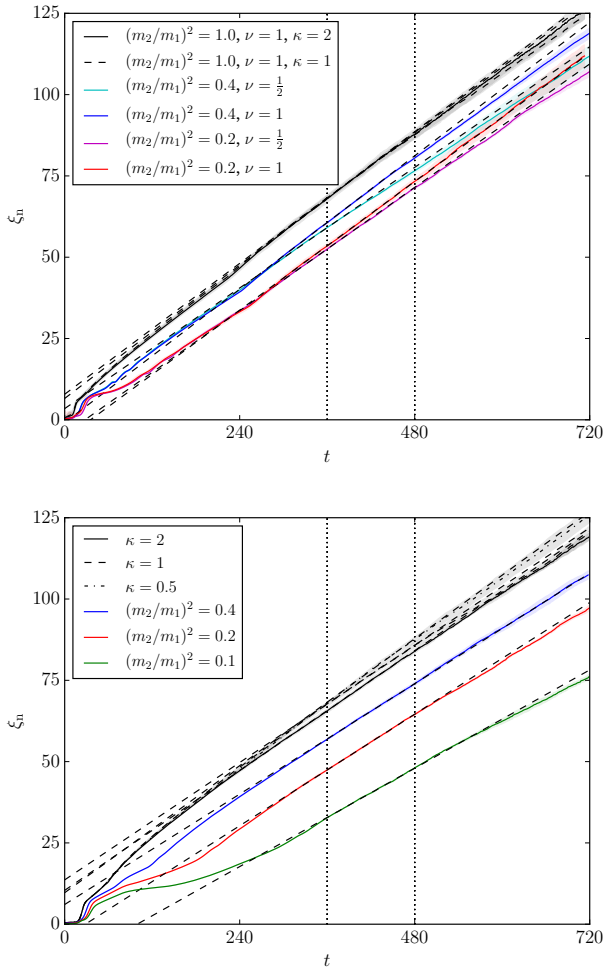


FIG. 2. Plot of the network length scale ξ_n , defined in Eq. (16), with core growth parameter $s = 1$ (top) and $s = 0$ (bottom). Fits to linear growth are also shown, within the range indicated by the vertical dashed lines. The gradients of the fit are given in Tables III and IV.

constant at large time. Hence the comoving separation of the monopoles remains the same order of magnitude as its value at the formation of the strings.

There is some evidence for a slow increase in n for the degenerate cases $m_2^2/m_1^2 = 1$ at $s = 1$, which may be due to semipole annihilations being less probable than monopole-antimonopole annihilations – some pairings of semipoles cannot annihilate [32]. However, the increase occurs after a half-light crossing time for the simulation box, so this may be a finite volume effect.

We illustrate the ability of semipoles to avoid annihilation in Fig. 5, which depicts two strings winding around the periodic lattice when the total length of string and the semipole number has stabilised. One can see that on one of the strings, the semipole density is much higher, and examination of multiple snapshots prior to this one

m_1^2	m_2^2	κ	ν	ξ_n gradient
0.25	0.25	2	1	0.171 ± 0.002
0.25	0.25	1	1	0.168 ± 0.004
0.25	0.1	1	0.5	0.154 ± 0.001
0.25	0.1	1	1	0.171 ± 0.002
0.25	0.05	1	0.5	0.158 ± 0.002
0.25	0.05	1	1	0.165 ± 0.004

TABLE III. Gradients for the network comoving length scale ξ_n , from the fits shown in the graphs of ξ_n against conformal time t for $s = 1$ in Fig. 2 (top).

m_1^2	m_2^2	κ	ξ_n gradient
0.1	0.1	2	0.154 ± 0.005
0.1	0.1	1	0.150 ± 0.003
0.1	0.1	0.5	0.163 ± 0.008
0.1	0.04	1	0.141 ± 0.004
0.1	0.02	1	0.143 ± 0.001
0.1	0.01	1	0.126 ± 0.001

TABLE IV. Gradients for the network comoving length scale ξ_n , from the fits shown in the graphs of ξ_n against conformal time t for $s = 0$ in Fig. 2 (bottom).

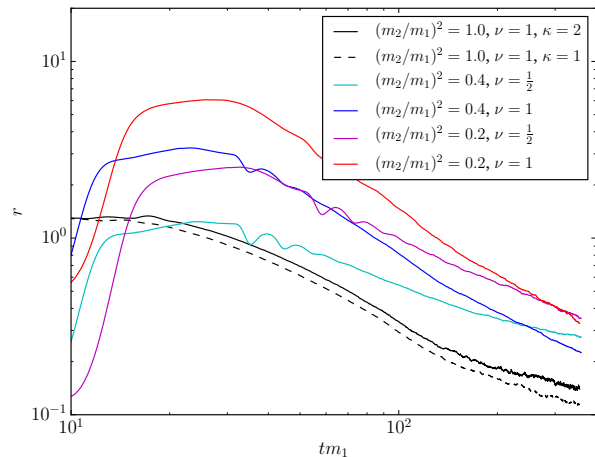


FIG. 3. The ratio of monopole to string energy density (3) in simulations with $s = 1$. The legend gives the expansion rate parameter $\nu = d \log a / d \log t$, the mass ratio of the fields m_2/m_1 , and in the degenerate case the value of the cross-coupling κ , which is otherwise $\kappa = 1$. The mass parameter $m_1^2 = 0.25$.

shows that semipoles have repelled each other. However, the high semipole density may be an artefact of the periodic boundary conditions, which have prevented the strings from shrinking in length any further. Without this shrinking, semipoles are not forced together, so there is less likelihood of overcoming the repulsion and

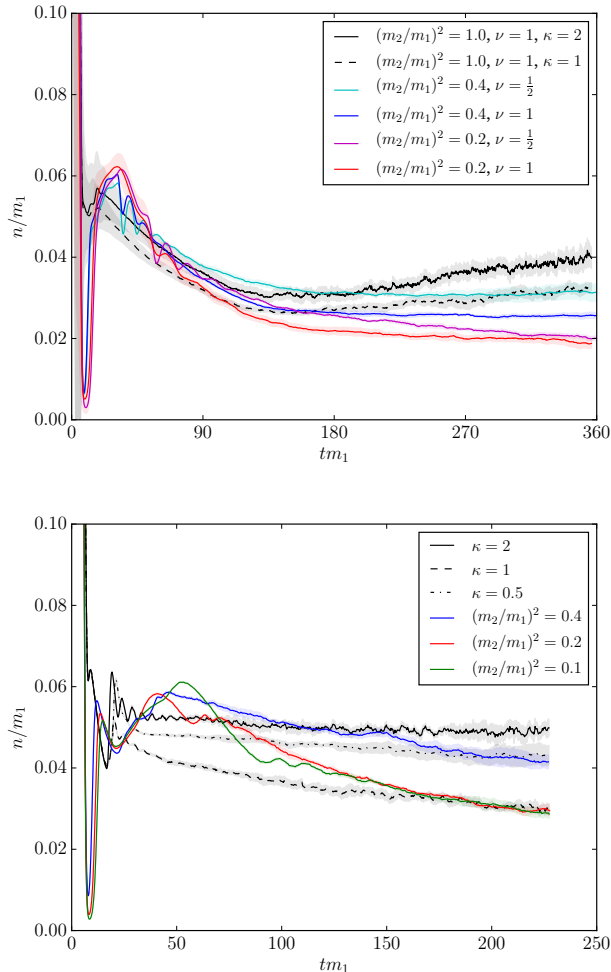


FIG. 4. The number of monopoles per comoving string length in simulations with $s = 1$ (top) and $s = 0$ (bottom). The legend gives the expansion rate parameter $\nu = d \log a / d \log t$, the mass ratio of the fields m_2/m_1 , and in the degenerate case the value of the cross-coupling κ , which is otherwise $\kappa = 1$. The mass parameter $m_1^2 = 0.25$ ($s = 1$) and $m_1^2 = 0.1$ ($s = 0$).

annihilating.

In the degenerate cases $m_2^2/m_1^2 = 1$ with $\kappa = 1$, we recall that the recorded monopole positions are just places where the phase of the complexified scalar has the value $\theta = \pm\pi/2$. The fact that the comoving distance between these points remains approximately constant indicates that the comoving RMS current is constant, and so the physical RMS current decreases in inverse proportion to the scale factor.

In the $s = 0$ case, the increased dynamic range means we can attempt a meaningful fit to investigate the relaxation to the constant n evolution. In Fig. 6, we show a graph of $n - n_\infty$, where the asymptotic value of the linear monopole density n_∞ is taken from a fit to the functional

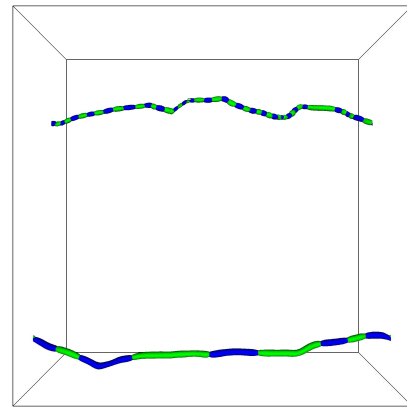


FIG. 5. A small 360^3 box at $t = 1080$, simulated at $m_2^2/m_1^2 = 1$ and $\kappa = 2$. The high density of semipoles on one of the strings shows that semipoles can avoid annihilation in some cases.

m_1^2	m_2^2	$\frac{n_\infty}{m_1}$	A	B
0.1	0.04	0.036	0.031	0.0072
0.1	0.02	0.023	0.060	0.0104
0.1	0.01	0.025	0.075	0.0134

TABLE V. Parameters for the fit of the linear monopole density data in Fig. 6 to the function (17). All simulations are radiation era, with $s = 0$.

form

$$n = n_\infty + A \exp(-B m_1 t). \quad (17)$$

Fits are shown with dashed lines, and fit parameters are given in Table V.

The fits confirm the visual impression that the linear monopole density is asymptoting to a constant non-zero value, and also support the exponential ansatz for the relaxation.

C. Monopole velocities

Fig. 7 shows the RMS velocities of the strings, monopoles and semipoles for different masses, cross-couplings κ , and expansion rate parameters ν . The RMS velocities all appear to asymptote at the same rate d_{BV}^{-1} to a constant value.

We see that the RMS string velocities are all around 0.5. When the field mass parameters m_1 and m_2 are different, the RMS monopole velocities are also all about 0.5, independent of the mass ratio and the expansion rate. If the mass parameters are the same, the RMS monopole velocity at about 0.63 is a little higher than the RMS string velocity. RMS velocities are consistent between $s = 1$ and $s = 0$, with the exception of the

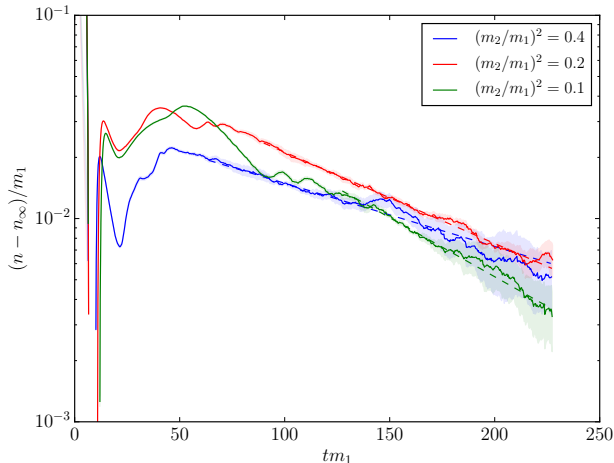


FIG. 6. The difference of the linear monopole density n from its asymptotic value n_∞ . The parameter n_∞ is extracted from a fit of n to a constant to exponential decay [see Eq. (17)]; the fits are shown as dashed lines. Both n and the time are scaled by m_1 to make dimensionless quantities. Only those values of m_2/m_1 where a reliable fit is possible are shown; for other values, the change in n is too small.

semipoles at $s = 0$, which appear to move a little slower ($\bar{v}_m \simeq 0.6$) than at $s = 1$ ($\bar{v}_m \simeq 0.68$).

The higher velocities of the semipoles should make collisions more frequent than those between monopoles and antimonopoles. However, as observed in the Introduction, semipole collisions need not result in annihilation, and so the higher velocities do not necessarily result in a lower monopole density.

We interpret the difference $\bar{v}_{\text{rel}}^2 = \bar{v}_m^2 - \bar{v}^2$ as the mean square relative velocity of the monopoles and semipoles along the string. One can estimate that, for semipoles, $\bar{v}_{\text{rel}} \simeq 0.3$, while there is little evidence for relative motion of monopoles.

VI. CONCLUSIONS

We have carried out simulations of non-Abelian cosmic strings, formed by the symmetry-breaking scheme $SU(2) \rightarrow Z_2$ by two adjoint scalar fields. This theory has classical solutions which can be interpreted as 't Hooft-Polyakov monopoles or semipoles [32] threaded by non-Abelian strings. We observe the formation of cosmic necklaces, consisting of networks of strings and monopoles or semipoles.

Our simulations were carried out in a cosmological background corresponding to a radiation dominated era, and also one with half the expansion rate of a radiation-dominated universe, testing the effect of the expansion rate. We performed simulations both with the true expanding universe equations of motion, and allowing the

cores of the topological defects to grow with the expansion of the universe. Core growth has been shown not to significantly affect the dynamics of strings [14, 15, 35], but its effect on the dynamics of necklaces is important to check.

In all cases, our numerical results are consistent with the evolution towards a scaling network of necklaces, with both the density of strings and the density of monopoles proportional to t^{-2} . We obtain scaling with or without core growth, giving confidence that scaling is a robust feature of a necklace network. A necklace network should therefore contribute a constant fraction to the energy density of the universe.

We observe that the number of monopoles per unit comoving length of string n changes little from its value at the formation of the string network: monopole annihilation on the string is therefore not as efficient as envisaged in Ref. [33], and the average comoving separation of monopoles along the string $d = 1/n$ remains approximately constant. The monopole to string density ratio r therefore decreases in inverse proportion to the scale factor, and does not increase as proposed in Ref. [30]. The RMS monopole velocity is close to the RMS string velocity, implying that the monopoles have no significant motion along the string. In particular, the suggestion that the monopole RMS velocity should be 50% larger than the string RMS velocity [33], due to the extra degree of freedom or motion, is not supported.

The number per unit comoving length of semipoles is also approximately constant in the simulations with core growth, but grows slightly in the simulations using the true equations of motion. We do not have large enough dynamic range to establish whether this is a finite volume effect. The semipole RMS velocity is higher than the string RMS velocity, indicating some relative motion of the semipoles along the string. Annihilation is still inefficient despite the relative motion, indicating that repulsion between semipoles is an important factor in the dynamics.

In the special case where the strings carry a supercurrent, the comoving distance between points where the Φ_1 field vanishes d also stays approximately constant. The supercurrent along the string can be estimated as $j \sim 1/ad$, where a is the scale factor, and should therefore decrease. This suggests that current is lost from shrinking loops of string, which would tend to prevent the formation of cosmologically disastrous stable string loops [42–44].

We are restricted to simulating necklace configurations with $r \sim 1$, so we are not able to fully test the robustness of the of the constant comoving d scaling regime. Nonetheless, we find it interesting to explore the consequences as it was not anticipated in previous dynamical modelling, which envisaged that d would either shrink to the string width [30], or grow with the horizon size [33]. The absence of a significant relative velocity between monopoles and strings indicates that monopoles are dragged around by the strings, independent of the

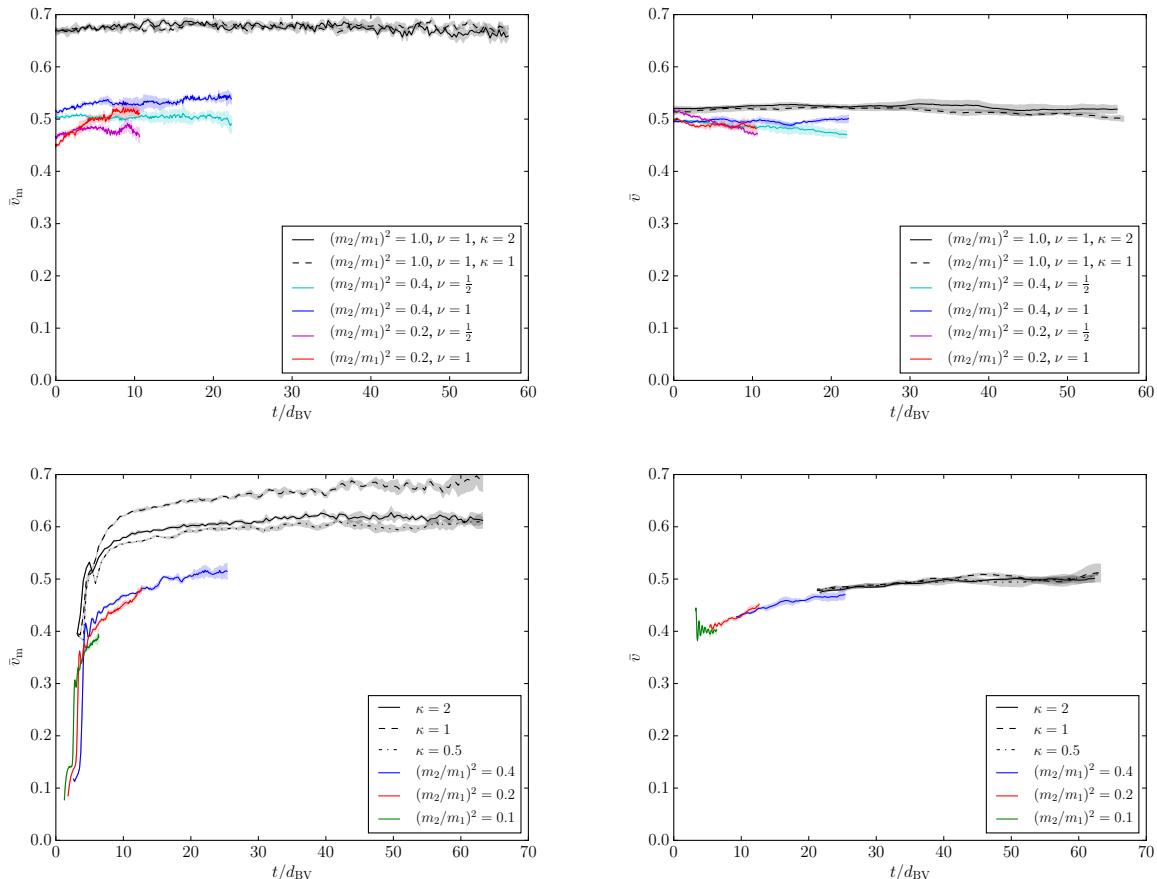


FIG. 7. Plot of \bar{v} and \bar{v}_m , the root mean square string and monopole/semipole velocities, for $s = 1$ (top) and $s = 0$ (bottom). The time axis is scaled by d_{BV} , defined in Eq. (2).

ratio of the energy scales. The average string separation is of order the conformal time t , which means that loops of string shrink and annihilate on that timescale. We infer that the main monopole annihilation channel is through collisions on shrinking loops of string.

As argued in [32], semipoles and monopoles are generic on strings in GUT models. It is interesting to consider their observational implications. As usual with strings, one must extrapolate the results of numerical simulations to a much larger ratio of the horizon size to the string width, and it is possible that subtle effects change the scaling of the network. It is clear in our simulations that, just as with Abelian Higgs strings, our $SU(2)$ strings lose energy efficiently into Higgs and gauge radiation. However, the process that causes the strings to emit radiation of massive Higgs and gauge fields is not well understood, and it may not be efficient over the huge range of scales between today's horizon size and the width of a GUT string. In this case, a necklace would end up behaving like ideal Nambu-Goto strings connecting massive particles, as assumed in [30] and [33].

In the case where field radiation is efficient, there is

little difference between a network of GUT strings with monopoles or semipoles and an Abelian Higgs string network. The network length scale grows in proportion to the horizon, and its energy density remains a constant fraction of the total. The energy is lost to massive particles, which (if coupled to the Standard Model) will show up in the diffuse γ -ray background. Current observations from Fermi-LAT indicate that the mass per unit length in Planck units $G\mu$ is bounded above by $3 \times 10^{-11} f_{\text{SM}}^{-1}$, where f_{SM} is the fraction of the strings energy ending up in γ -rays [45]. This fraction is likely to be close to unity in a GUT theory, and so such strings are essentially ruled out, as observed some time ago [12]. However, strings in a hidden sector are subject only to constraints from the Cosmic Microwave Background [46–48], which are $G\mu \lesssim 10^{-7}$.

In the case where the string dynamics eventually changes over to Nambu-Goto, the difference between a necklace network and an ordinary cosmic string network is more dramatic with our new picture that the comoving distance between monopoles remains approximately constant from the time the strings formed. For GUT

scale strings forming along with the monopoles, this is bounded above by the horizon distance at the GUT temperature, or a few metres today. Even if the scale of the U(1) symmetry-breaking is as low as a TeV, this distance is $O(10^{12})$ m today, a factor 10^{-14} smaller than the horizon size. When horizon-size string loops are chopped off the long string network, they will therefore have a large number of monopoles on them. Numerical investigations indicate [49] that such string loops do not have periodic non-self-intersecting solutions. We can therefore expect them to quickly chop themselves up into smaller and smaller loops, some of which will be free of monopoles and find stable periodic non-self-intersecting trajectories. In this case, the typical loop size for a GUT scale string would be a few metres rather than the horizon size. Hence, the tight bounds on the Nambu-Goto string tension from msec pulsar timing obtained by the European Pulsar Timing Array [50] and NANOGrav [51] would be avoided, as the gravitational waves would be at frequencies inaccessible to direct observation.

ACKNOWLEDGMENTS

We acknowledge fruitful discussions with Jarkko Järvelä during the initial stages of this project. Our simulations made use of the COSMOS Consortium supercomputer (within the DiRAC Facility jointly funded by STFC and the Large Facilities Capital Fund of BIS). DJW was supported by the People Programme (Marie Skłodowska-Curie actions) of the European Union Seventh Framework Programme (FP7/2007-2013) under grant agreement number PIEF-GA-2013-629425. MH acknowledges support from the Science and Technology Facilities Council (grant number ST/L000504/1).

Appendix A: Equations of motion on the lattice

We write the adjoint Higgs field as $\Phi_n = \phi_n^a \tau^a$, with $n = 1, 2$. The link variables for the gauge field are $U_\mu = u^0 1 + i u^a \sigma^a$, with $u^a \in \mathbb{R}$.

The $d = 4$ continuum action in a FLRW background with scale factor a and $s = 1$ is

$$S = \int d^4x \left(-\frac{1}{4} F_{\mu\nu}^a F^{\mu\nu a} + a^2 \sum_n \text{Tr}[D_\mu, \Phi_n][D^\mu, \Phi_n] - a^4 V(\Phi_1, \Phi_2) \right) \quad (\text{A1})$$

where indices are raised with the Minkowski metric $\eta_{\mu\nu} = \text{diag}(1, -1, -1, -1)_{\mu\nu}$.

As discussed both in Section III and in Appendix B below, in order to mitigate the shrinking of the string and monopole cores in comoving coordinates one can allow the coupling constants and mass parameters to become time-dependent,

$$m_{1,2}^2 \rightarrow \frac{m_{1,2}^2}{a^{2(1-s)}}, \quad \lambda \rightarrow \frac{\lambda}{a^{2(1-s)}}, \quad g \rightarrow \frac{g}{a^{2(1-s)}}. \quad (\text{A2})$$

The physical string and monopole core widths can be set to grow by choosing $s < 1$, with $s = 0$ maintaining constant comoving core widths. This completely avoids the possibility of the topological defects shrinking in size below the lattice spacing, although the effect on their dynamics must be checked. In this paper we have used $s = 1$ and $s = 0$ only.

With this in mind, we take the lattice action to be

$$\begin{aligned} S[U, \Phi] = & \frac{4}{g^2 a^{2(s-1)}} \sum_{x; i} \left[1 - \frac{1}{2} \text{Tr} U_{0i}(x) \right] - \frac{4}{g^2 a^{2(s-1)}} \sum_{x; i < j} \left[1 - \frac{1}{2} \text{Tr} U_{ij}(x) \right] \\ & + \sum_{x; n} a^2 \text{Tr}[D_0, \Phi_n][D_0, \Phi_n] - \sum_{x; i, n} a^2 \text{Tr}[D_i, \Phi_n][D_i, \Phi_n] - \sum_x a^4 V(\Phi_1, \Phi_2) \end{aligned} \quad (\text{A3})$$

with unit comoving lattice spacing and scale factor a . The covariant derivative is

$$[D_\mu, \Phi_n](x) = U_\mu(x) \Phi_n(x + \hat{\mu}) U_\mu^\dagger(x) - \Phi_n(x). \quad (\text{A4})$$

In the temporal gauge $U_0(x) = 1$,

$$\begin{aligned} S[U, \Phi] = & \frac{4}{g^2 a^{2(s-1)}} \sum_{x; i} \left[1 - \frac{1}{2} \text{Tr} U_{0i}(x) \right] - \frac{4}{g^2 a^{2(s-1)}} \sum_{x; i < j} \left[1 - \frac{1}{2} \text{Tr} U_{ij}(x) \right] \\ & + \sum_{x; n} a^2 \text{Tr} \dot{\Phi}_n^2 - \sum_{x; i, n} a^2 \left[2 \text{Tr} \Phi_n^2 - 2 \text{Tr} \Phi_n(x) U_i(x) \Phi_n(x + \hat{i}) U_i^\dagger(x) \right] - \sum_x a^4 V(\Phi_1, \Phi_2) \end{aligned} \quad (\text{A5})$$

and after a Legendre transformation, the full Hamiltonian is

$$H(t) = \frac{1}{2g^2 a^{2(s-1)}} \sum_{x,i,a} \epsilon_i^a(x,t)^2 + \frac{1}{2} a^2 \sum_{x;n,a} \pi_n^a(x,t)^2 + \frac{4}{g^2 a^{2(s-1)}} \sum_{x;i < j} \left(1 - \frac{1}{2} \text{Tr} U_{ij}(x,t) \right) - a^2 \sum_{x;i,n} 2 \text{Tr} \Phi_n(x) U_i(x) \Phi_n(x+\hat{i}) U_i^\dagger(x) + a^2 \sum_{x,n} 6 \text{Tr} \Phi_n^2 + a^4 \sum_x V(\Phi_1, \Phi_2). \quad (\text{A6})$$

The equations of motion on the lattice are (recalling that we use the label a for elements of the Lie algebra and n to label separate fields)

$$g^2 a^{2(s-1)} \frac{\partial}{\partial t} \left(\frac{\epsilon_i^a(\mathbf{x}, t)}{g^2 a^{2(s-1)}} \right) = - \sum_{j \neq i} \text{Tr} \{ i \sigma^a U_{ij}(\mathbf{x}, t) \} + g^2 a^{2s} \sum_n \left[-i \text{Tr} \left\{ \Phi_n(\mathbf{x}, t) \sigma^a U_i(\mathbf{x}, t) \Phi_n(\mathbf{x} + \hat{i}, t) U_i^\dagger(\mathbf{x}, t) \right\} + i \text{Tr} \left\{ \Phi_n(\mathbf{x}, t) U_i(\mathbf{x}, t) \Phi_n(\mathbf{x} + \hat{i}, t) U_i^\dagger(\mathbf{x}, t) \sigma^a \right\} \right] \quad (\text{A7})$$

$$\dot{U}_i(\mathbf{x}, t) = -i \epsilon_i(\mathbf{x}, t) U_i(\mathbf{x}, t) \quad (\text{A8})$$

$$\frac{1}{a^2} \frac{\partial}{\partial t} (a^2 \pi_n^a(\mathbf{x}, t)) = 6 \phi_n^a + a^2 \frac{\partial V(\Phi_1, \Phi_2)}{\partial \phi_n^a} - \sum_j \text{Tr} \left[\sigma^a U_j(\mathbf{x}, t) \Phi_n(\mathbf{x} + \hat{j}, t) U_j^\dagger(\mathbf{x}, t) \right] - \sum_j \text{Tr} \left[\sigma^a U_j^\dagger(\mathbf{x} - \hat{j}, t) \Phi_n(\mathbf{x} - \hat{j}, t) U_j(\mathbf{x} - \hat{j}, t) \right] \quad (\text{A9})$$

$$\dot{\phi}_n^a(\mathbf{x}, t) = \pi_n^a(\mathbf{x}, t) \quad (\text{A10})$$

where, for example

$$\frac{\partial V(\Phi_1, \Phi_2)}{\partial \phi_1^a} = \frac{1}{a^{2(1-s)}} \left[m_1^2 \phi_1^a + 2\lambda (\text{Tr} \Phi_1^2) \phi_1^a + \kappa (\text{Tr} \Phi_1 \Phi_2) \phi_2^a \right], \quad (\text{A11})$$

and similarly for ϕ_2^a .

The Gauss law is

$$G(x) = \sum_i \text{Re Tr} \sigma^a \left(\epsilon_i(x) - U_i^\dagger(x-\hat{i}) \epsilon_\nu(x-\hat{i}) U_i(x-\hat{i}) \right) - \rho(x) = 0 \quad (\text{A12})$$

where the scalar charge density $\rho(x)$ is

$$\rho(x) = 2g^2 a^{2s} \sum_n \text{Tr} \sigma^a (\Pi_n \Phi_n - \Phi_n \Pi_n). \quad (\text{A13})$$

1. Remarks on the numerical implementation

The implicit damping terms in Eqs. (A7, A9) are handled by a method of the Crank-Nicolson type [52]. For Eq. (A7), let us write the right hand side as $F\{U_i(x, t), \Phi(x, t)\}$. Then we have

$$\dot{\epsilon}_i^a + 2(1-s) \frac{\dot{a}}{a} \epsilon_i^a = F\{U_i(x, t), \Phi(x, t)\}, \quad (\text{A14})$$

which can be discretised as

$$\frac{\epsilon_i^a(t + \delta t/2) - \epsilon_i^a(t - \delta t/2)}{\delta t} + (1-s) \frac{a(t + \delta t/2) - a(t - \delta t/2)}{\delta t a(t + \delta t/2)} [\epsilon_i^a(t + \delta t/2) + \epsilon_i^a(t - \delta t/2)] = F\{U_i(x, t) \Phi(x, t)\}. \quad (\text{A15})$$

A similar expression can then be found for Eq. (A9).

The gauge field evolution equation (A8) can be solved to give

$$U_i(x, t + \delta t) = \exp \left\{ -i \frac{\sigma^j}{2} \epsilon_i^j(x, t + \delta t/2) \delta t \right\} U_i(x, t). \quad (\text{A16})$$

We carry out a period of cooling prior to the core growth (in $s = 1$) or Hubble (in $s = 0$) phases. The coupling constants and scale factor are kept constant, and damping terms $\sigma\epsilon$ and $\sigma\pi_n^a$ are added to Eqs. (A7) and (A9) respectively. This particular choice preserves the Gauss law. We needed to use a very small timestep $\delta t = 0.025$ during this short cooling phase.

Appendix B: Simulation in an expanding universe: core growth

In the comoving coordinates of the lattice, the cores of defects shrink as a^{-1} , where a is the cosmological scale factor, as the simulation proceeds. If the lattice resolution is to be sufficient to resolve the core widths at the end of the simulation, the core would be larger than the simulation box size L in the initial conditions. The core widths are also related to the time for the fields to relax to their minima, making the production of a defect network from random initial conditions hard to achieve.

To address the problem we scale the parameters of the theory by powers of a^{1-s} , with $0 \leq s \leq 1$, as in Eq. (9). This makes the comoving widths of the strings and monopoles w_s and w_m proportional to a^{-s} . At $s = 0$, the comoving width is constant. The properties of Abelian Higgs string networks are largely independent of s , as they are controlled by the string tension, which is invariant under this scaling [14, 15, 35].

In order to simulate at $s = 1$, we control s through the simulation so that the core width is small in the initial conditions, and grows to meet the physical core width at a controllable time t_{cg} . The core widths of the strings and monopoles in our $s = 1$ simulations are plotted in Fig. 8.

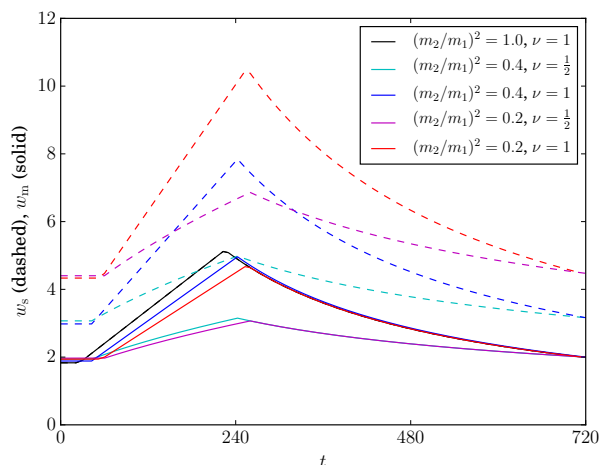


FIG. 8. Comoving core widths of monopoles (w_m , solid) and strings (w_s , dashed) in the $s = 1$ simulations. The core widths are defined as $w_m = (am_1)^{-1}$ and $w_s = (am_2)^{-1}$, where a is the scale factor.

Appendix C: Projectors, magnetic charge, and winding number

In this Appendix, we follow Ref. [40] in denoting the two Higgs fields in the adjoint representation by Φ and χ . We will assume that $\Phi = \Phi_1$ forms the 't Hooft-Polyakov monopoles, while $\chi = \Phi_2$ is responsible for the strings.

We define the projectors $\Pi_{\pm} = \frac{1}{2}(1 \pm \hat{\Phi})$, where $\hat{\Phi} = \Phi\sqrt{2/\text{Tr}\Phi^2}$ (similarly, $\hat{\chi} = \chi\sqrt{2/\text{Tr}\chi^2}$).

1. Magnetic charge

For the time being, in this section we will return to the full 4-dimensional theory.

In the symmetry broken phase, a residual U(1) symmetry persists. We can derive link variables u_{μ} corresponding to this smaller gauge group [40, 53],

$$u_{\mu}(x) = \Pi_{+}(x)U_{\mu}(x)\Pi_{+}(x + \hat{\mu}); \quad (\text{C1})$$

these can be shown to transform like the Abelian gauge field. The corresponding Abelian field strength tensor is

$$A_{\mu\nu} = \arg \text{Tr} u_{\mu}(x)u_{\nu}(x + \hat{\mu})u_{\mu}^{\dagger}(x + \hat{\nu})u_{\nu}^{\dagger}(x) \quad (\text{C2})$$

and, with the correct factors of the coupling to give a continuum electromagnetic field,

$$\alpha_{\mu\nu} = \frac{2}{g}A_{\mu\nu} \quad (\text{C3})$$

$$= \frac{2}{g} \arg \text{Tr} u_{\mu}(x)u_{\nu}(x + \hat{\mu})u_{\mu}^{\dagger}(x + \hat{\nu})u_{\nu}^{\dagger}(x) \quad (\text{C4})$$

and, finally, the expression for the lattice magnetic field

$$B_i = \frac{1}{2}\epsilon_{ijk}\alpha_{jk}. \quad (\text{C5})$$

The symmetry breaking phase transitions studied in this work allow the creation of magnetic charge. On the lattice, the projected Gauss law for the magnetic field takes the form

$$\sum_{i=1}^3 [B_i(x + \hat{i}) - B_i(x)] = \rho_M(x) = \frac{4\pi N}{g} \quad (\text{C6})$$

where N is an integer. It is important to note that the magnetic charge is quantised and localised within lattice cells.

2. Winding number

The above section yielded $\alpha_{\mu\nu}$, the analogue of the Abelian gauge field, and hence E_i and B_i . To measure the winding number directly [40], we also need to find the equivalent of the Abelian Higgs field, as its phase angle appears in the definition of winding number.

The difference in phase angle for the residual Higgs field at neighbouring lattice sites $(x, x + \hat{i})$ is then

$$\delta_i(x) = \arg \text{Tr} [\hat{\chi}(x)\Pi_-(x)U_i(x)\Pi_-(x + \hat{i})\hat{\chi}(x + \hat{i})\Pi_+(x + \hat{i})U_i^\dagger(x)\Pi_+(x)]. \quad (\text{C7})$$

The winding number through a plaquette is then

$$Y_{ij}(x) = \delta_i(x) + \delta_j(x + \hat{i}) - \delta_i(x + \hat{j}) - \delta_j(x) - 2A_{ij}(x) \quad (\text{C8})$$

which is gauge-invariant.

We then approximate the string length L in the system by the total string winding through all plaquettes,

$$\sum_{x;i < j} Y_{ij}(x) = 2\pi L. \quad (\text{C9})$$

-
- [1] T. Kibble, *J.Phys.* **A9**, 1387 (1976).
[2] M. Hindmarsh and T. Kibble, *Rept.Prog.Phys.* **58**, 477 (1995), arXiv:hep-ph/9411342 [hep-ph].
[3] A. Vilenkin and E. P. S. Shellard, *Cosmic Strings and Other Topological Defects* (Cambridge University Press, 2000).
[4] E. J. Copeland, L. Pogosian, and T. Vachaspati, *Class.Quant.Grav.* **28**, 204009 (2011), arXiv:1105.0207 [hep-th].
[5] M. Hindmarsh, *Prog.Theor.Phys.Suppl.* **190**, 197 (2011), arXiv:1106.0391 [astro-ph.CO].
[6] H. B. Nielsen and P. Olesen, *Nucl.Phys.* **B61**, 45 (1973).
[7] E. Witten, *Phys.Lett.* **B153**, 243 (1985).
[8] S. Sarangi and S. H. Tye, *Phys.Lett.* **B536**, 185 (2002), arXiv:hep-th/0204074 [hep-th].
[9] E. J. Copeland, R. C. Myers, and J. Polchinski, *JHEP* **0406**, 013 (2004), arXiv:hep-th/0312067 [hep-th].
[10] J. Lizarraga and J. Urrestilla, *JCAP* **1604**, 053 (2016), arXiv:1602.08014 [astro-ph.CO].
[11] P. Laguna and R. Matzner, *Phys.Rev.Lett.* **62**, 1948 (1989).
[12] G. Vincent, N. D. Antunes, and M. Hindmarsh, *Phys.Rev.Lett.* **80**, 2277 (1998), arXiv:hep-ph/9708427 [hep-ph].
[13] J. Moore, E. Shellard, and C. Martins, *Phys.Rev.* **D65**, 023503 (2002), arXiv:hep-ph/0107171 [hep-ph].
[14] N. Bevis, M. Hindmarsh, M. Kunz, and J. Urrestilla, *Phys.Rev.* **D75**, 065015 (2007), arXiv:astro-ph/0605018 [astro-ph].
[15] N. Bevis, M. Hindmarsh, M. Kunz, and J. Urrestilla, *Phys.Rev.* **D82**, 065004 (2010), arXiv:1005.2663 [astro-ph.CO].
[16] T. Vachaspati and A. Vilenkin, *Phys. Rev.* **D35**, 1131 (1987).
[17] E. J. Copeland and P. M. Saffin, *JHEP* **11**, 023 (2005), arXiv:hep-th/0505110 [hep-th].
[18] M. Hindmarsh and P. Saffin, *JHEP* **0608**, 066 (2006), arXiv:hep-th/0605014 [hep-th].
[19] J. Urrestilla and A. Vilenkin, *JHEP* **0802**, 037 (2008), arXiv:0712.1146 [hep-th].
[20] L. Leblond and M. Wyman, *Phys. Rev.* **D75**, 123522 (2007), arXiv:astro-ph/0701427 [astro-ph].
[21] C. J. A. P. Martins, *Phys. Rev.* **D82**, 067301 (2010), arXiv:1009.1707 [hep-ph].
[22] M. Hindmarsh and T. Kibble, *Phys.Rev.Lett.* **55**, 2398 (1985).
[23] H. J. de Vega and F. A. Schaposnik, *Phys. Rev. Lett.* **56**, 2564 (1986).
[24] H. J. de Vega and F. A. Schaposnik, *Phys. Rev.* **D34**, 3206 (1986).
[25] M. Aryal and A. E. Everett, *Phys. Rev.* **D35**, 3105 (1987).
[26] T. W. B. Kibble, G. Lazarides, and Q. Shafi, *Phys. Lett.* **B113**, 237 (1982).
[27] R. Jeannerot, J. Rocher, and M. Sakellariadou, *Phys. Rev.* **D68**, 103514 (2003), arXiv:hep-ph/0308134 [hep-ph].
[28] G. 't Hooft, *Nucl. Phys.* **B79**, 276 (1974).
[29] A. M. Polyakov, *JETP Lett.* **20**, 194 (1974), [*Pisma Zh. Eksp. Teor. Fiz.*20,430(1974)].
[30] V. Berezinsky and A. Vilenkin, *Phys.Rev.Lett.* **79**, 5202 (1997), arXiv:astro-ph/9704257 [astro-ph].
[31] T. W. B. Kibble and T. Vachaspati, *J. Phys.* **G42**, 094002 (2015), arXiv:1506.02022 [astro-ph.CO].
[32] M. Hindmarsh, K. Rummukainen, and D. J. Weir, *Phys. Rev. Lett.* **117**, 251601 (2016), arXiv:1607.00764 [hep-th].
[33] J. J. Blanco-Pillado and K. D. Olum, *JCAP* **1005**, 014 (2010), arXiv:0707.3460 [astro-ph].
[34] P. Forgacs, N. Obadia, and S. Reuillon, *Phys.Rev.* **D71**, 035002 (2005), arXiv:hep-th/0412057 [hep-th].
[35] D. Daverio, M. Hindmarsh, M. Kunz, J. Lizarraga, and J. Urrestilla, *Phys. Rev.* **D93**, 085014 (2016), arXiv:1510.05006 [astro-ph.CO].
[36] A. Rajantie, *Phys. Rev.* **D79**, 043515 (2009), arXiv:0810.3007 [astro-ph].
[37] P. B. Arnold, *Phys. Rev.* **D55**, 7781 (1997), arXiv:hep-ph/9701393 [hep-ph].
[38] G. D. Moore, *Nucl. Phys.* **B480**, 689 (1996), arXiv:hep-lat/9605001 [hep-lat].
[39] M. Hindmarsh, K. Rummukainen, T. V. I. Tenkanen, and D. J. Weir, *Phys. Rev.* **D90**, 043539 (2014), arXiv:1406.1688 [hep-lat].
[40] A. Davis, T. Kibble, A. Rajantie, and H. Shanahan, *JHEP* **0011**, 010 (2000), arXiv:hep-lat/0009037 [hep-lat].
[41] R. J. Scherrer and A. Vilenkin, *Phys. Rev.* **D58**, 103501 (1998), arXiv:hep-ph/9709498 [hep-ph].
[42] J. P. Ostriker, A. C. Thompson, and E. Witten, *Phys. Lett.* **B180**, 231 (1986).
[43] E. J. Copeland, N. Turok, and M. Hindmarsh, *Phys. Rev. Lett.* **58**, 1910 (1987).
[44] R. L. Davis and E. P. S. Shellard, *Nucl. Phys.* **B323**, 209

- (1989).
- [45] H. F. Santana Mota and M. Hindmarsh, Phys. Rev. **D91**, 043001 (2015), arXiv:1407.3599 [hep-ph].
 - [46] A. Moss and L. Pogosian, Phys. Rev. Lett. **112**, 171302 (2014), arXiv:1403.6105 [astro-ph.CO].
 - [47] T. Charnock, A. Avgoustidis, E. J. Copeland, and A. Moss, Phys. Rev. **D93**, 123503 (2016), arXiv:1603.01275 [astro-ph.CO].
 - [48] J. Lizarraga, J. Urrestilla, D. Daverio, M. Hindmarsh, and M. Kunz, JCAP **1610**, 042 (2016), arXiv:1609.03386 [astro-ph.CO].
 - [49] X. Siemens, X. Martin, and K. D. Olum, Nucl.Phys. **B595**, 402 (2001), arXiv:astro-ph/0005411 [astro-ph].
 - [50] L. Lentati et al., Mon. Not. Roy. Astron. Soc. **453**, 2576 (2015), arXiv:1504.03692 [astro-ph.CO].
 - [51] Z. Arzoumanian et al. (NANOGrav), Astrophys. J. **821**, 13 (2016), arXiv:1508.03024 [astro-ph.GA].
 - [52] J. Crank and P. Nicolson, Advances in Computational Mathematics **6**, 207 (1996).
 - [53] S. Edwards, D. B. Mehta, A. Rajantie, and L. von Smekal, Phys.Rev. **D80**, 065030 (2009), arXiv:0906.5531 [hep-lat].